VOXEL-BASED MODELING OF AIRFLOW IN THE HUMAN NASAL CAVITY

Shinya Kimura[a]* , Takashi Sakamoto[a], Toshihiro Sera[b], Hideo Yokota[c], Kenji Ono[d], Denis J. Doorly[e], Robert C. Schroter[f] and Gaku Tanaka[a]

[a]Graduate School of Engineering, Chiba University, Chiba, Japan; [b]Department of Mechanical Engineering, Kyushu University, Fukuoka, Japan; [c]Image Processing Research Team, RIKEN Center for Advanced Photonics, Saitama, Japan; [d]Interdisciplinary Computational Science Section, Research Institute for Information Technology, Kyushu University, Fukuoka, Japan; [e]Department of Aeronautics, and [f]Department of Bioengineering, Imperial College London, London SW7 2AZ, UK

Shinya Kimura

Graduate School of Engineering, Chiba University, 1-33 Yayoi-cho, Inage-ku, Chiba 263-8522, Japan

Takashi Sakamoto

Graduate School of Engineering, Chiba University, 1-33 Yayoi-cho, Inage-ku, Chiba 263-8522, Japan

Toshihiro Sera

Department of Mechanical Engineering, Kyushu University, 744 Motooka, Nishi-ku, Fukuoka 819-0395, Japan

Hideo Yokota

Image Processing Research Team, RIKEN Center for Advanced Photonics, 2-1 Hirosawa, Wako, Saitama 351-0198, Japan

Kenji Ono

Research Institute for Information Technology, Kyushu University, 744 Motooka, Nishi-ku, Fukuoka 819-0395, Japan

Denis J. Doorly

Department of Aeronautics, Imperial College London, London SW7 2AZ, UK

Robert C. Schroter

Department of Bioengineering, Imperial College London, London SW7 2AZ, UK

Gaku Tanaka

Graduate School of Engineering, Chiba University, 1-33 Yayoi-cho, Inage-ku, Chiba 263-8522, Japan

+81-43-290-3180

gtanaka@faculty.chiba-u.jp

VOXEL-BASED MODELING OF AIRFLOW IN THE HUMAN NASAL CAVITY

This paper describes the simulation of airflow in human nasal airways using voxel-based modeling characterized by robust, automatic, and objective grid generation. Computed tomography scans of a healthy adult nose are used to reconstruct 3D virtual models of the nasal airways. Voxel-based simulations of restful inspiratory flow are then performed using various mesh sizes to determine the level of granularity required to adequately resolve the airflow. For meshes with close voxel spacings, the model successfully reconstructs the nasal structure and predicts the overall pressure drop through the nasal cavity.

Keywords: computational fluid dynamics; voxel-based simulation; human nasal cavity.

Introduction

As part of the upper respiratory system, the nasal airways perform several functions from the nasal cavity to the trachea. Sensing odorant molecules and filtering pollutants and airborne particles across the nasal mucosa are the main functions relevant to transporting and absorbing particles. As the air-conditioning function, inspired air is heated and humidified by the blood vessels in the mucosa layer over the short distance from the nostrils to the nasopharynx for the protection of the lower respiratory tract (Elad et al. 2008). Because the intricate anatomy of the nasal cavity makes it difficult to predict detailed airflow patterns in vivo (Lang 1989), physical models derived from medical images have been used in computational studies (Keyhani et al. 1995; Kumahata et al. 2010; Bates et al. 2014) to determine the detailed patterns of nasal airflow. Thus, it has been demonstrated that CFD is useful for understanding the characterization of nasal airflow. Therefore, applying CFD methods to assessment of surgical intervention is considered (Zhao et al. 2006a, 2006b; Garcia et al. 2007).

To express a realistic nasal cavity shape as a computational grid in CFD, boundary-fitted grids can be used. This method accurately reconstructs the complex geometry of the nasal cavity using thin boundary layers allocated along the surface. However, this technique requires high-quality grid generation, because the calculation accuracy depends on the quality of the grid. When adapted for complex nose-like geometries, grid generation becomes difficult and requires expertise and experience. For example, significant manual intervention is required to fix the distortion of the reconstructed surface grids, especially where the medical image resolution is relatively low in the nasal anatomy. Under these artificially reconstructed surface grids, the quality of the boundary-fitted grid depends on the operator. Therefore, time-consuming operation and reliance on the skill of the operator become significant issues when using CFD for medical assistance.

The present study investigates the potential for volume pixel (voxel)-based modeling of airflow in the nasal cavities to provide a quantitative evaluation of nasal air-conditioning in individual subjects. Voxel-based simulations use a Cartesian structured grid. This method is characterized by robust, automatic, and objective grid generation, which can be easily obtained from medical images with no operator variability (Handbook 2003). The shape of the voxel-based computational grid model can be modified directly by changing the arrangement of solid and fluid cells without remeshing. These characteristics are beneficial for medical assistant tools using CFD. In addition, large-scale parallel computation using a Cartesian data structure has demonstrated good performance (Ono et al. 2014). Therefore, voxel-based approaches are suitable for large-scale airflow modeling in the nasal cavity, such as direct numerical simulations. Although the Cartesian grid method enables low-cost mesh generation,

shape approximation errors and a lack of resolution in the boundary layer can be problematic.

The uniform Cartesian grid method requires a huge number of grid cells besides the boundary-fitted grid to completely resolve the velocity boundary layer. Adaptive mesh refinement or Cartesian cut-cell methods offer a potential solution for reducing the huge number of cells, but the time-marching and efficiency of the parallel computations will become worse because the Courant-Friedrichs-Lewy (CFL) number is limited by the smallest-volume cell of these methods. When using high-performance computing, the efficiency of the parallel operations should be prioritized.

In this study, the mesh refinement required to adequately resolve the airflow in the nasal cavities using this grid method is evaluated through a comparison with the boundary-fitted grid method.

Computational grid generation

There are several ways to reconstruct 3D model-enabled numerical analysis from medical images. Figure 1 shows the reconstruction procedures for the Cartesian grid method and boundary-fitted grid method. The nasal cavity model was reconstructed using 240 CT slices (the axial direction at an image resolution of 0.488 mm × 0.488 mm and a slice interval of 0.400 mm) of a healthy 51-year-old male with no clinical disorders (Figure 2(a)) , which was approved by the Third Research Ethics Committee of RIKEN.

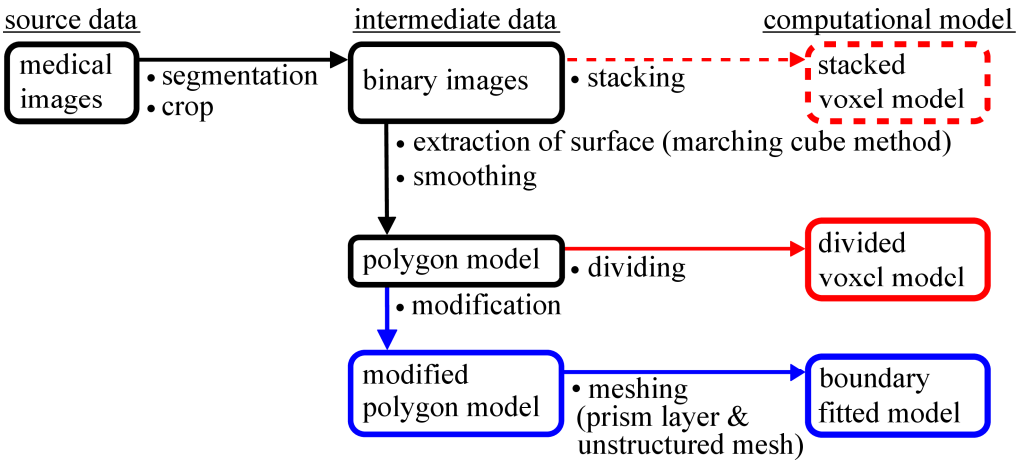

Figure 1. Flowchart of the reconstruction of 3D computational models. Black solid lines indicate the flow of the common method. Red solid lines indicate the proposed method. Red dotted lines indicate the proposed method not considered in this study. Blue lines indicate the comparative method.

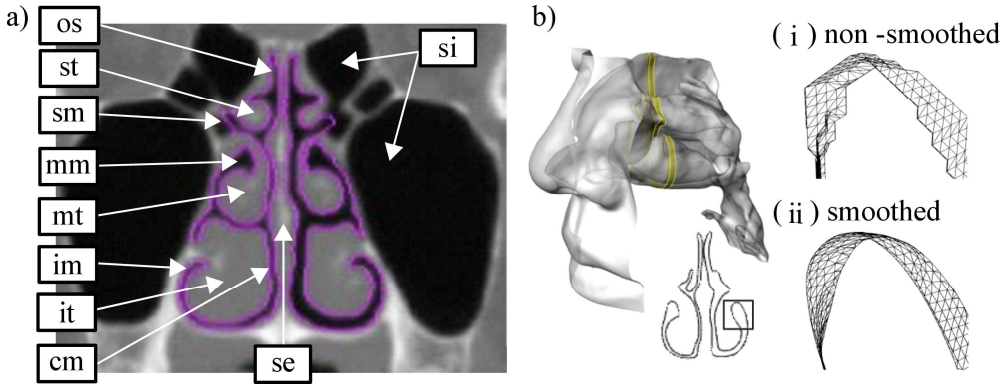

Figure 2. Procedure for polygon model generation. (a) CT images: os, olfactory slit; st, superior turbinate; sm, superior meatus; mm, middle meatus; mt, middle turbinate; im, inferior meatus; it, inferior turbinate; cm, common meatus; se, septum; si, sinus; (b) polygon model.

First, the virtual surfaces of the nasal airway and external face boundaries were defined using commercially available image segmentation software (Amira Ver. 5.2.2, Visage Imaging) applied to the CT image dataset. Segmentation was almost automatic using a threshold brightness level. However, significant manual user intervention was required to define the complex network around the superior turbinate and sinus, where

the CT images cannot resolve the boundary precisely. Finally, an ear, nose, and throat surgeon reviewed the airway reconstructions to ensure their fidelity. These segmented images were converted to binary images and cropped to 240 slices with a resolution of 240 x 120 pixels, equivalent to the calculation domain from the front of the face to the throat. The cropped binary images were then placed into a 3D polygon model using a marching cube algorithm (Figure 2(b)). The polygon model exhibits defects such as holes, gaps, overlaps, or sharp edges when the image resolution is insufficient. These defects must be manually modified by CAD if the polygon model is to be used in the boundary-fitted method. Depending on the resolution of the CT images, the polygon model was filtered using a smoothing algorithm (Taubin 1995) to remove roughness and provide physiological (idealized) smooth surfaces.

Secondly, the two voxel grid generation methods described below were applied. The simplest technique is stacked voxel grid generation, which converts each binary pixel into a three-dimensional binary voxel grid by stacking the binary images. This method is appropriate for medical applications because it involves less manipulation and operator dependence. As the simplest approximation, the boundary between the fluid and solid cells is constructed using a binary voxel. As binary voxels have stepwise surfaces, we must consider how to resolve the boundary layer. Basically, the resolution of the computational grid is equal to the image resolution, because each pixel in an image corresponds to a single voxel. Although it is possible to generate a finer computational grid than the image resolution, the form of the computational model does not change accordingly because it is dependent on the resolution of the source images. This dependence on the image resolution is a weakness of this technique.

A second approach is the divided voxel grid generation method, which divides the polygon model into predetermined voxel grids to diminish the effect of image

resolution. In the bounding box surrounding the polygon model, each cell is assigned as either solid or fluid according to whether it is located inside or outside the polygon. Therefore, no mesh-refinement is necessary for this method. Because the polygon model interpolates the surface geometry so that the final resolution is finer than the image resolution, the resolution effect is diminished when the voxel size is less than the image resolution. To verify the effect of reducing the influence of the initial resolution, it was confirmed that the convergence and value of the predicted pressure drops using half-resolution images made from the same CT scans are almost the same.

Nevertheless, although this method prepares a polygon model, the grid generation cost of the voxel grid method is less than the boundary-fitted grid method. In this study, the divided voxel grid generation method was adopted to take advantage of the effect of image resolution.

Figure 3 illustrates the divided voxel grid generation method. The voxel generation processes were performed using V-Xgen ver. 1.5 and V-Xpp ver. 1.5, developed by the VCAD System Research Program at RIKEN. These applications were integrated into FFV-C, which is a three-dimensional unsteady incompressible thermal flow simulator integrated with a Cartesian grid generator (available from https://github.com/avr-aics-riken/ffvc_package). The bounding box defines the computational domain divided into uniform arbitrary voxels and surrounds the polygon model. Because a finer voxel pitch model has a smoother surface, eight different voxel pitch values were evaluated (0.1, 0.2, 0.3, 0.4, 0.5, 0.8, 1.0, and 1.5 mm). Each of the voxels has an ID indicating whether it is a fluid or solid cell and a value indicating the volume fraction (VF) of fluid. Voxels on the solid side were assigned VF values of 0 (0/255), those on the other side were assigned VF values of 1 (255/255), and those on the boundary between fluid and solid were assigned VF values from 1/255 to 254/255.

Therefore, the airway volume of the voxel model in this method has up to ±0.2% discretization error. In this study, to minimize the volume change of boundary voxels between fluid and solid, the medium ID of each voxel was set to fluid when VF > 0.5; other voxels were set to be solid. As the simplest approximation, the boundary between fluid and solid cells was constructed from binary voxels, which have stepwise surfaces. The number of cells in each voxel pitch is listed in Table 1.

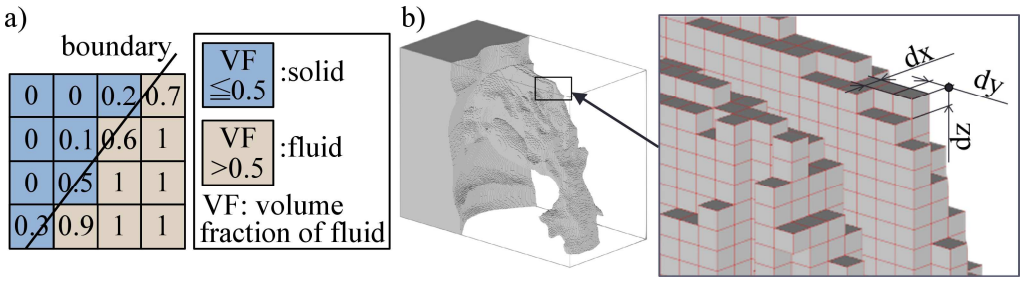

Figure 3. Procedure for computational grid generation: (a) boundary definition of voxelization; (b) voxel grid of the nasal airway.

Table 1. Number of voxels

voxel pitch	total cell	fluid cell
1.5	171,288	7,858
1.0	576,288	26,794
0.5	4,650,048	219,268
0.2	72,825,092	3,440,369
0.1	579,911,670	122,754,625

For comparison, the boundary-fitted grid was generated via the polygon model. Commercial grid generation software (Gambit and T-Grid, ANSYS Japan K.K.) was used to produce unstructured hybrid meshes from the 3D polygon model, combining interior tetrahedral elements with a multi-layered pentahedral (prism) mesh adjacent to the nasal wall. To ensure that the computational predictions of pressure loss were independent of the density of the computational mesh, the grid convergence was analyzed. Eventually, three layers of near-wall prism cells were constructed. The thickness of each prism layer was constrained to 0.1 mm to ensure accurate flow predictions in the near-wall region. The total number of cells was 4.5 million.

Boundary-fitted grid refinements generally require several hours (e.g. 1 h in this study) when the polygon model has no defects, whereas Cartesian grid generations reduces this by an order of magnitude to several minutes (e.g. less than 1 min with a voxel pitch of 0.2 mm). If the polygon model has any defects, the necessary modifications may take several hours (e.g. 8 h in this study). If there are too many defects, it may not be possible to create computational grids. In contrast, even if the polygon model has many defects, Cartesian grid generation is feasible, making our method particularly robust.

Regarding the boundary-fitted method, grid-refinement occupies roughly one third of the overall time—in this study, segmentation of medical images takes 8 h, grid refinement (modification of the polygon model and grid generation) takes 9 h, and then the calculation takes 8 h. The Cartesian grid method can decrease the percentage required for grid generation to <5% because it does not require the polygon model to be free of defects. Thus, the segmentation of medical images still takes 8 h and the calculation also takes 8 h, but grid generation typically requires several minutes. These process times are rough estimations based on our study: the actual process time of the

segmentation and CAD modification will depend on the experience of the operator and the medical image resolution, because the polygon model will have more defects if the image resolution is coarser. The calculation time depends on the computer and parallel performance.

CFD method

For the simulation of restful inspiratory flow in the nasal cavities, the governing equations for the conservation of mass and momentum in 3D incompressible laminar unsteady flow were solved using FFV-C ver. 2.1.5 thermo-fluid solver (RIKEN).

$$\frac{\partial u_i}{\partial x_i} = 0 \tag{1}$$

$$\frac{\partial u_i}{\partial t} + \frac{\partial}{\partial x_j}(u_i u_j) = -\frac{1}{\rho}\frac{\partial P}{\partial x_i} + \nu \frac{\partial}{\partial x_j}[(\frac{\partial u_i}{\partial x_j} + \frac{\partial u_j}{\partial x_i})] \tag{2}$$

where ρ and ν denote the density and kinematic viscosity of air at 25°C, respectively. In these formulations, the coupling between the pressure and velocity field was implemented through a fractional step method using a collocated grid finite volume formulation. Poisson's pressure equation was solved using the Successive Over-Relaxation (SOR) method. The third-order Monotone Upwind Scheme for Conservation Laws (MUSCL) method was employed for the spatial discretization of the advection term, and the first-order forward Euler method was used for the time integration. The scaled residual of velocity during the solution process was required to converge to below 10^{-3}. The time step was determined using a Courant–Friedrichs–Lewy (CFL) number of 0.1 and a maximum velocity of 5 m/s at the throat. Figure 4 shows the boundary condition used in this study. A traction-free condition (Gresho 1991a, 1991b)

was imposed at the entrance to the bounding box upstream of the model as the outer boundary condition, and a constant inspiratory flow rate of 230 ml/s was imposed at the throat as the inner boundary condition. The traction-free condition is expressed as

$$T_{ij} n_j = 0 \tag{3}$$

$$T_{ij} = -P\delta_{ij} + \mu\left(\frac{\partial u_i}{\partial x_j} + \frac{\partial u_j}{\partial x_i}\right) \tag{4}$$

where T_{ij} is the inner stress tensor, n_j is the normal to the outer boundary, and P is the gauge pressure, which is assumed to be zero in the far field. Allowing the flow to develop naturally towards the nostril, the external area was set to 60 mm wide, 94 mm high (45 mm from nasal tip to bottom of outer boundary), and 20 mm deep from the nasal tip. The walls of the nasal cavity were assumed to be rigid, and the no-slip boundary condition was applied along this surface. In the boundary-fitted grid method, the governing equations described above were solved using a commercial CFD package (Fluent Ver. 6.3.26; ANSYS Japan K.K.) with a second-order segregated flow solver based on the SIMPLE method. The Reynolds numbers at the nasal valve, based on the hydraulic diameter of the minimum cross-sectional area, were 835 on the left and 586 on the right.

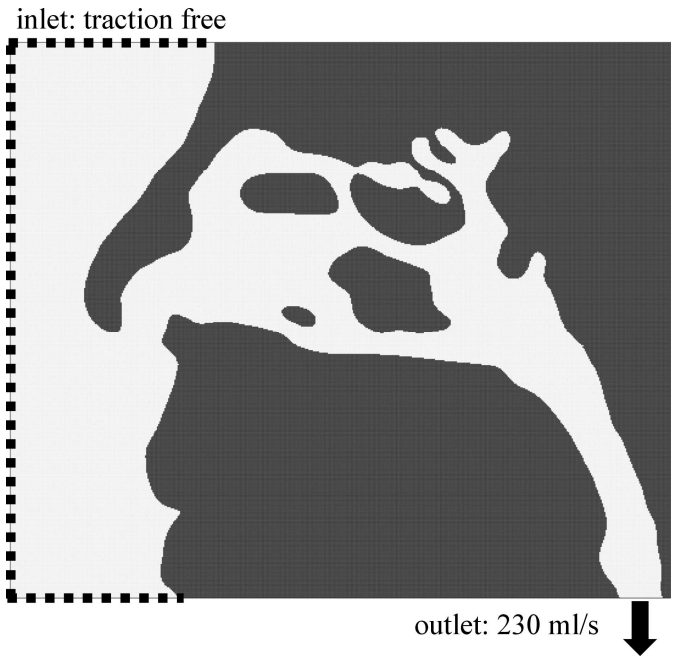

Figure 4. Boundary condition and computational domain.

Anatomy

Figure 5 shows details of the nasal airway. In this model, though the perimeter through each cavity is almost the same, there are significant asymmetric differences in the structure of the right and left cavities, with the left cross-sectional area approximately 1.4 times larger than that in the right. This is an effect of structural differences, the nasal cycle, or reactions to allergens/infections (Eccles 2000). The nasal airways are separated by the septum, which is composed of cartilage tissue. The left and right hydraulic diameters (= 4×area/perimeter) at the nasal valve in plane 2, where the cross-sectional area often attains a minimum, are 8.2 mm and 8.9 mm. The nasal airway extends vertically at its posterior to the nasal valve. The turbinate region consists of a slit-like common meatus connected to the superior, middle, and inferior meatus between planes 4 and 6. The upper part of the common meatus contains the olfactory epithelium, which contains sensory nerve endings for smell. Both airways join at plane 8 before the

nasopharynx at plane 9. The paranasal sinuses surrounding the nasal cavity are connected via small orifices. In this study, the paranasal sinuses were excluded from the computational domain. Thus, this complex anatomy is characteristic of the nasal cavity. To estimate the geometry of the nasal cavity quantitatively, the complexity is defined as:

$$(complexity) = \frac{l^2}{4\pi A} \tag{5}$$

where l is the perimeter and A is the cross-sectional area. Figure 4(d) shows the complexity distribution as a function of distance from the nose tip. The cross-section at plane 5 has the highest complexity of 37, which is equivalent to gathering this number of parallel tubes, although the nasal cavity has only two passages.

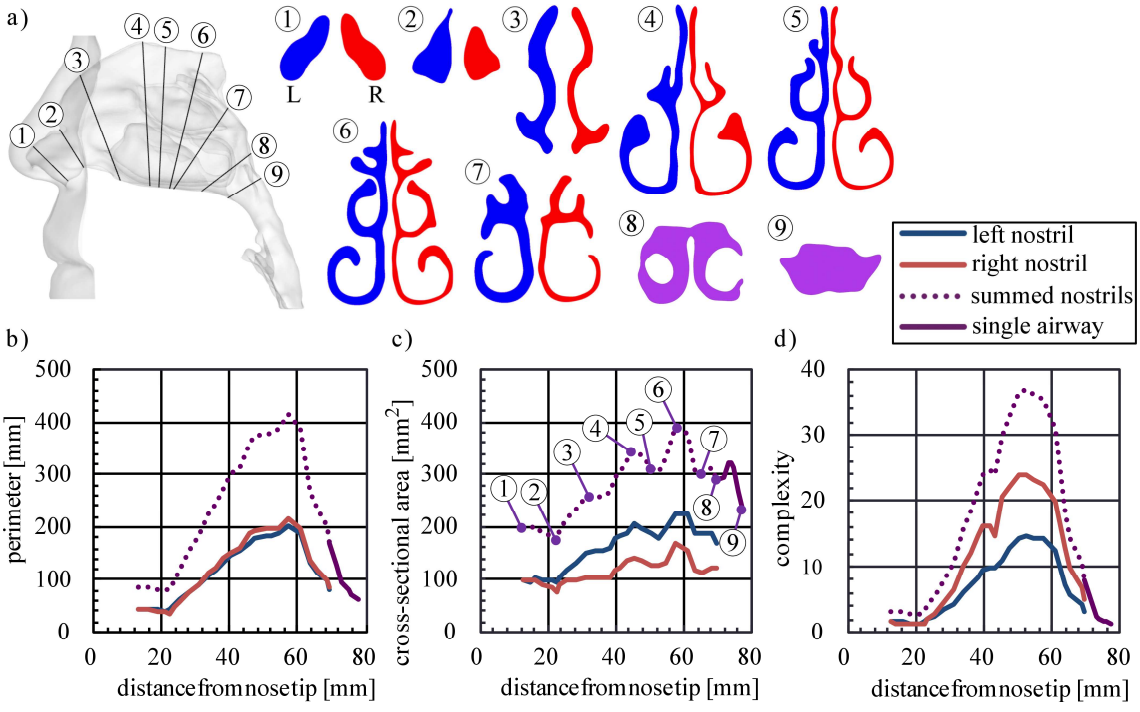

Figure 5. Geometry of the nasal airway: (a) geometry of flow-normal cross-sections; (b) perimeter distribution; (c) area distribution; (d) complexity distribution.

Results and discussion

Figure 6 shows the coronal cross-section of each voxel pitch model at plane 5, where has the most complex shape. The left and right cavities of the voxel model are colored blue and red, respectively. Black lines indicate the boundary of the polygon model. When the voxel pitch is above 1.0 mm, the cavities are barely divided by the septum. Moreover, the narrow right inferior and common meatus are not resolved correctly when the voxel pitch is above 1.0 mm. Figure 7 shows the percentage error of the volume and surface area of the voxel model with respect to the polygon model. The percentage errors of volume with a voxel pitch of 0.4 mm or less are below 0.2%, which is equivalent to the discretization error. In contrast, regardless of voxel pitch, the surface area of the voxel model is overestimated by more than 40% owing to the stepwise surface of the binary voxels. Because the left and right cavities connect with each other at larger voxel pitches, the error in the surface area becomes relatively smaller; this is not a reflection of the reproduction accuracy. Therefore, the voxel model requires a voxel pitch of 0.4 mm or less to successfully reconstruct the nasal cavity structure (although not its surface area). Though there are methods to improve the reproduction accuracy of the boundary, they are not considered in this study.

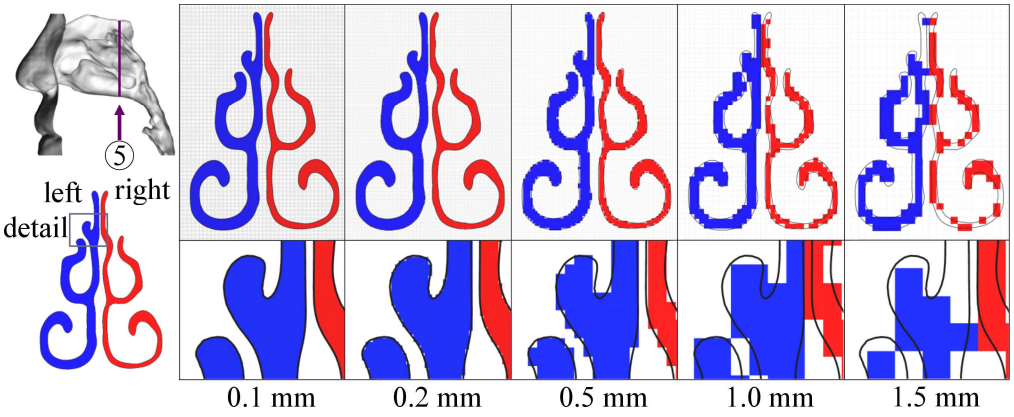

Figure 6. Comparison of airways for each voxel pitch.

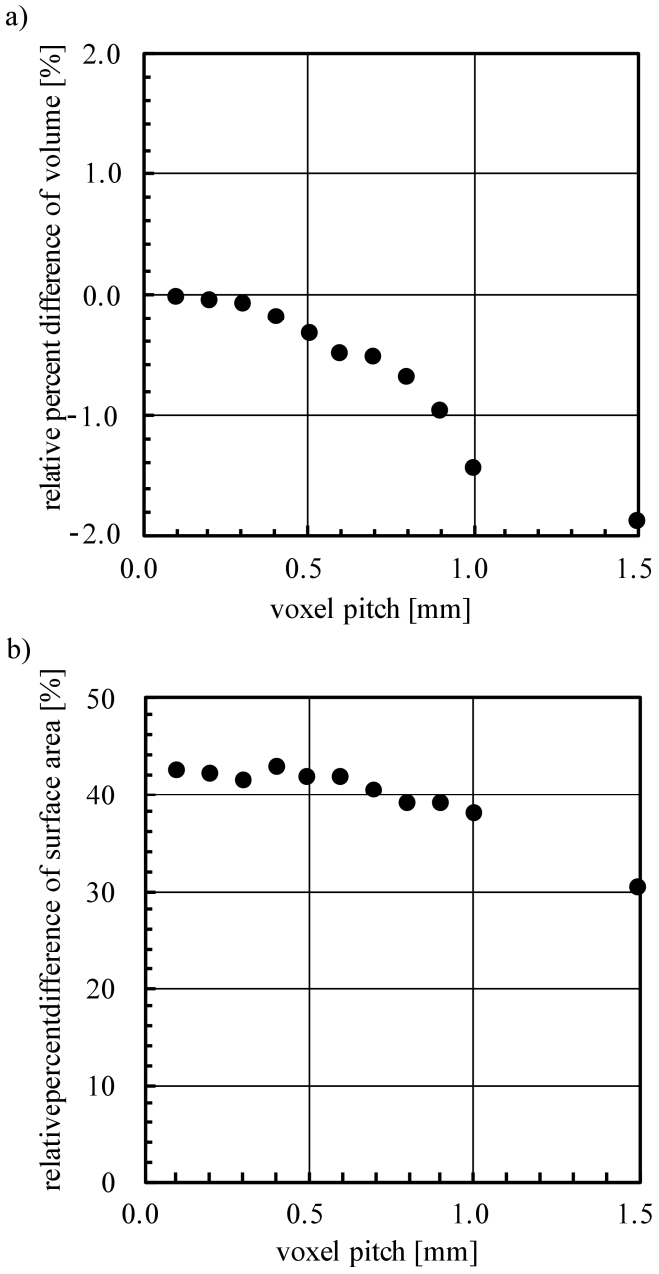

Figure 7. Volume and surface area of model for each voxel pitch.

The effect of the voxel pitch on computational predictions is confirmed by the convergence of pressure loss through the nasal airway. Figure 8 shows the simulated pressure drop between the nostril and nasopharynx as a function of voxel pitch. The pressure drop decreases with the voxel pitch because of the smoother surface. The pressure drop is overestimated with a larger voxel pitch because the rough surface of the airway disturbs the flow features and provokes flow separation in the vicinity of the

wall. The pressure drop converges as the voxel pitch decreases, and is relatively constant for voxel pitches of 0.1–0.2 mm, with a difference in magnitude of 1.2%. Moreover, good agreement can be observed between the converged pressure drop and that obtained using the boundary-fitted model, which has a value of 10 Pa. This result indicates that the overestimation caused by the stepwise surface approximation can be ignored when the voxel pitch is sufficiently fine.

Figure 9 illustrates the velocity magnitude at the sagittal cross-sections indicated by blue lines. The velocity distribution in both simulation methods is in overall agreement, except at the throat. Figure 10 illustrates the magnitude of wall shear stress (WSS) from inner and outer side views of both nasal cavities with a voxel pitch of 0.2 mm and using the boundary-fitted model. The most of the WSS distributions given by the voxel method is consistent with one of the boundary-fitted method, except near the nasal valve and nasopharynx. The WSS is less than 0.19 Pa across over 95% of the intranasal surface area. WSS of magnitudes greater than 0.4 Pa is distributed near the nasal valve and nasopharynx, where the velocity of airflow is higher than in other areas. The friction velocity and non-dimensional wall distance are expressed as

$$u^* = \sqrt{\frac{\tau_w}{\rho}} \tag{6}$$

$$y^* = u^* \frac{y}{\nu} \tag{7}$$

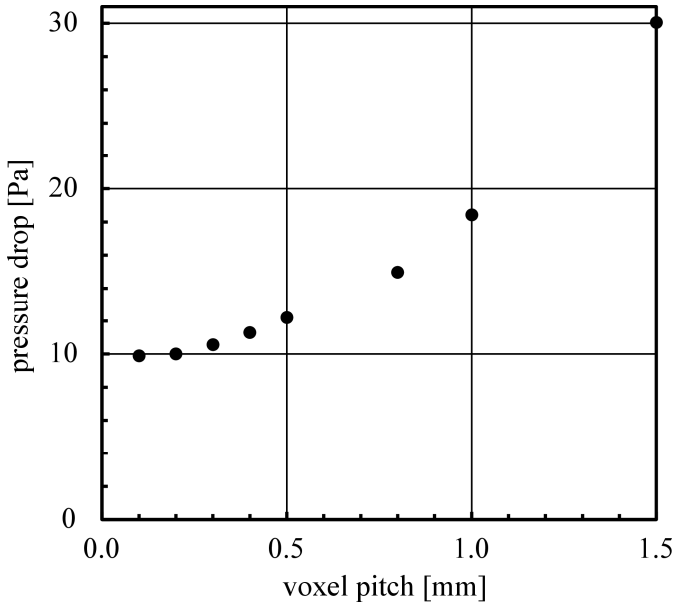

Figure 8. Total pressure drop between nostril and nasopharynx.

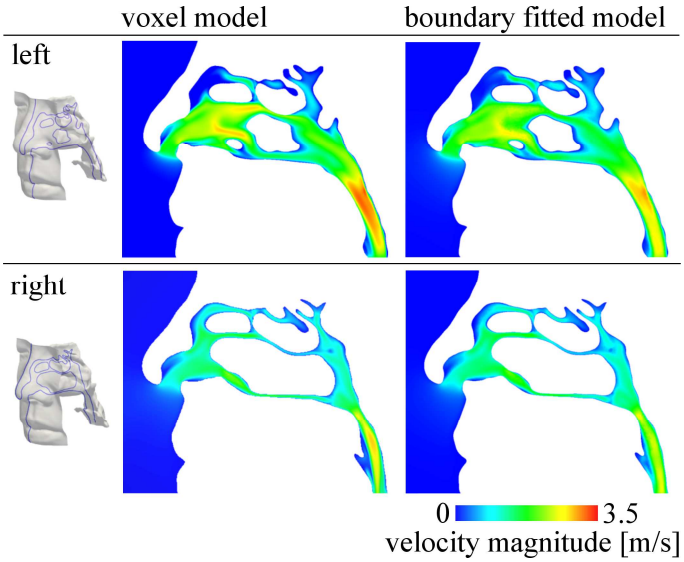

Figure 9. Velocity magnitude.

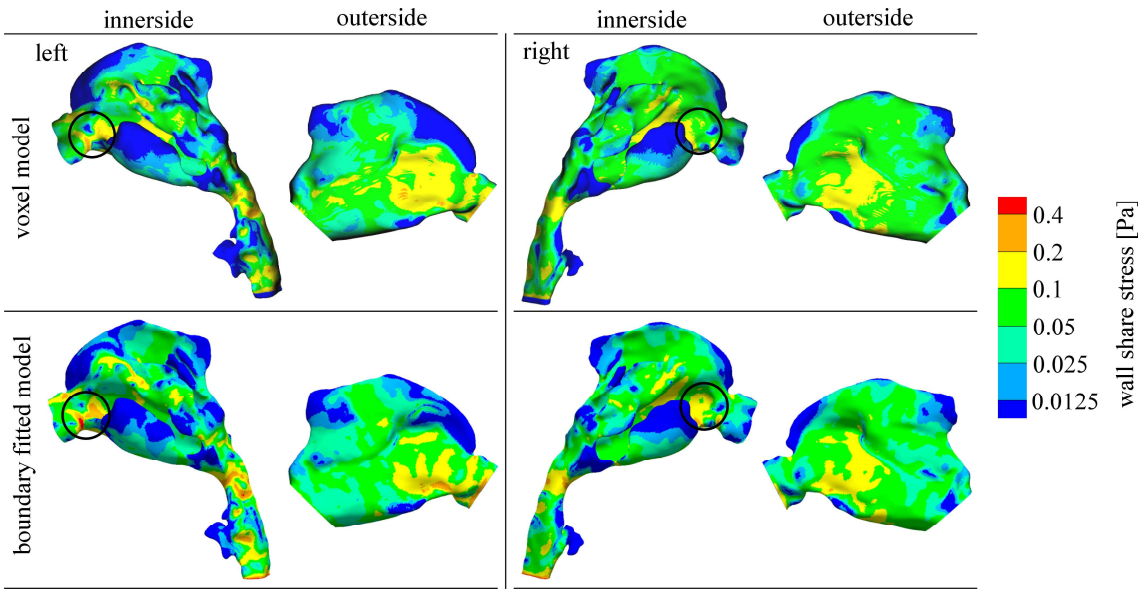

Figure 10. Magnitude of WSS.

When the voxel pitch is 0.2 mm and WSS = 0.19 Pa, the distance from the wall to the neighboring cell center is equivalent to y+ = 5. Because the thickness of the viscous sublayer generally has a y+ value less than 5, the intranasal surface with a voxel pitch of 0.2 mm can be regarded as hydraulically smooth, except near the nasal valve and nasopharynx. This estimation agrees with the convergence of pressure loss through the nasal airway. Therefore, a voxel pitch of approximately 0.2 mm is sufficient for reliable computations of the overall pressure drop.

We did not observe any unsteadiness in the flow at a flow rate of 230 ml/s; unsteadiness is not explicitly considered in this paper, but we have conducted simulations at higher flow rates of 370 ml/s and 500 ml/s and investigated the relationship between pressure loss and flow rate. It was confirmed that the airflow is stable until a flow rate of 370 ml/s and that the pressure loss increases rapidly above this flow rate. Some unsteadiness in the flow was observed in the upper nasal passage, near the olfactory slit of the left nasal cavity, at a flow rate of 500 ml/s. Further investigation is necessary to describe the flow transition with increasing flow rate. In future studies,

we will apply a finer voxel pitch using the K computer to obtain the unsteadiness characteristics of this modelling method.

Conclusion

Numerical simulations using a Cartesian grid were applied to steady inspiratory flow in the nasal cavity. A voxel-based model successfully reconstructed the nasal cavity structure from CT images, despite having a stepwise surface. The numerical predictions of pressure loss through the nasal cavity given by the voxel grid method correspond with those from the boundary-fitted method when the voxel pitch is 0.2 mm, except around the nasal valve, where the velocity boundary layer is less than half the voxel pitch. This suggests that, when the medical image is effectively resolved to less than 0.2 mm, the directly stacked voxel generation method gives sufficiently accurate pressure loss predictions for medical applications. Before using this method in practical applications, the number of subjects should be increased to ensure the generality of this approach.

Acknowledgments

The present study was supported by JSPS KAKENHI Grant Number 26630059 and JSPS Bilateral Program. This research used computational resources of the K computer provided by the RIKEN Advanced Institute for Computational Science through the HPCI System Research project (Project ID:hp160186).

Reference

Bates AJ, Doorly DJ, Cetto R, Calmet H, Gambaruto AM, Tolley NS, Houzeaux G, Schroter RC. 2014 Dec. Dynamics of airflow in a short inhalation. J R Soc Interface. 12:20140880

Eccles R. 2000 Aug. Nasal airflow in health and disease. Acta Oto-Laryngol. 120:580-595.

Elad D, Wolf M, Keck T. 2008 Nov. Air-conditioning in the human nasal cavity. Resp Physiol Neurobi. 163:121-127.

Garcia GJM, Bailie N, Martins DA, Kimbell JS. 2007 Aug. Atrophic rhinitis: a CFD study of air conditioning in the nasal cavity. J Appl Physiol. 103:1082-1092.

Gresho, P.M. 1991 Jan. Incompressible fluid dynamics: Some fundamental formulation issue. Annu Rev Fluid Mech. 23:413-453.

Gresho, PM. 1991 Jun. Some current CFD issues relevant to the incompressible Navier-Stokes equation. Comput Methods in Appl Mech Eng. 87:201-252.

Keyhani K, Scherer PW, Mozell MM. 1995 Nov. Numerical simulation of airflow in the human nasal cavity. J Biomech Eng. 117:429-441.

Kumahata K, Mori F, Ishikawa S, Matsuzawa T. 2010 Nov. Nasal flow simulation using heat and humidity models. J Biomed Sci Eng. 5:565-577.

Lang, J. 1989. Clinical anatomy of the nose, nasal cavity and paranasal sinuses. New York: Georg Thieme Verlag.

Ono K, Kawashima Y, Kawanabe T. 2014. Data Centric Framework for Large-scale High-performance Parallel Computation. 14th International Conference on Computational Science. 29:2336-2350.

Suchi ryutai rikigaku handobukku [Handbook of Numerical Fluid Dynamics]. 2003 Mar. Kobayashi T. Maruzen:586-591. Japanese.

Taubin G. 1995. Curve and surface smoothing without shrinkage. Proceedings of the 5th International Conference on Computer Vision; Jun 20-23; Cambridge, MA, USA; pp. 852–857; Washington DC: IEEE Computer Society Press.

Zhao K, Dalton P, Yang GC, Scherer PW. 2006 Dec. Numerical modeling of turbulent and laminar airflow and odorant transport during sniffing in the human and rat nose. Chem Sences. 31:107-118.

Zhao K, Pribitkin EA, Cowart BJ, Rosen D, Scherer PW, Dalton P. 2006 May-Jun. Numerical modelling of nasal obstruction and endoscopic surgical intervention: Outcome to airflow and olfaction. Am J Rhinol. 20:308-316.